Journal of Iberian Geology
https://doi.org/10.1007/s41513-018-0065-3

RESEARCH PAPER

$^{40}Ar/^{39}Ar$ chronological constraints on syn- and post-Variscan biotite porphyroblasts from the Iberian Chains, NE Spain

J. Javier Álvaro[1] · Blanca Bauluz[2] · Andrés Gil-Imaz[2] · Teresa Ubide[3]

Received: 11 December 2017 / Accepted: 4 May 2018

Abstract
We perform a multidisciplinary study of biotite porphyroblasts and veinlet infills hosted in Cambrian strata of the hanging walls from the NW-SE-trending Datos, Jarque and Daroca thrusts (Iberian Chains). Stratigraphic and microstructural crosscutting features indicate that a biotite isograd runs parallel to the southeastern transects of the three thrusts. The metamorphic grade reached in the southeastern edge of the Iberian Chains is clearly distinct from both the Cadomian epizonal metamorphism, exclusively recorded in the Ediacaran–basalCambrian Paracuellos Group, and the Variscan anchizone metamorphism recorded throughout Cambrian–Devonian strata. During post–Variscan negative inversion tectonics, renewed K-metasomatism along the same thrusts led to crystallisation of geochemically similar biotites in parallel fissures and veins. $^{40}Ar/^{39}Ar$ ages are (i) latest Westphalian–to–Guadalupian (285.82 ± 23.75 Ma) for metamorphic biotite porphyroblasts affected by diffusion loss of Ar, including the Carboniferous–Permian transition within error; and (ii) Early Triassic (246.87 ± 5.36 Ma) for biotite occlusion in post–Variscan veinlets. The Iberian Chains represent the southeastern prolongation of the Cantabrianand West Asturian-Leonese zones. The latter displays a uniform eastward decrease in metamorphic grade, whereas the Iberian Chains exhibits a heterogeneous distribution of low-grade metamorphic conditions (chlorite zone). The local presence of the biotite isograd is linked to the higher tectonic gradients associated with the Daroca, Jarque and Datos thrusts, quite similar to the metamorphic isogrades recognized both in the northeastern edge of the Demanda Massif and the Novellana-Pola de Allande-Degaña Belt of the West Asturian-Leonese Zone. This distribution allows the identification of a broad NW-SE belt of biotite-in isograd-related synkinematic metamorphism, following the western contact of the Narcea Antiform, the Anguiano Thrust and the southeastern edges of the Daroca, Jarque and Datos Thrusts in the Iberian Chains. Based on Variscan structural style and metamorphic grades, the Datos Thrust links with the contact that separates the Cantabrian and West Asturian-Leonese zones of the Iberian Massif.

Keywords Biotite · Porphyroblast · Isograd · Metasomatism · Gondwana

Resumen
Se presenta en este trabajo un análisis multidisciplinar de biotitas metamórficas (porfiroblastos) y metasomáticas (de relleno fisural) contenidas en pizarras y mármoles cámbricos que forman el bloque superior de los cabalgamientos deDaroca, Jarque y Datos en las Cadenas Ibéricas. Su contexto estratigráfico y microtectónico permite reconocer una isograda de la biotita situada paralelamente a la traza de los tres frentes de cabalgamiento, que representan tres estructuras variscas de primer orden con orientación NO-SE. La isograda de biotita, alcanzada en el extremo sudoriental de las Cadenas Ibéricas, es claramente diferenciable del metamorfismo epizonal cadomiense, exclusivamente reconocido en el Grupo de Paracuellos (Ediacárico–Cámbrico basal) y del grado regional de anquizona varisco registrado en el Cámbrico–Devónico. Los cabalgamientos citados experimentaron una inversión tectónica negativa post–varisca, a la que se asoció un metasomatismo potásico, responsable de la precipitación de biotitas geoquímicamente similares a las variscas, como relleno de fisuras y venas. Las edades de los porfiroblastos y rellenos fisurales de biotita, determinadas mediante el método de $^{40}Ar/^{39}Ar$, son

Electronic supplementary material The online version of this article (https://doi.org/10.1007/s41513-018-0065-3) contains supplementary material, which is available to authorized users.

Extended author information available on the last page of the article

Published online: 01 June 2018

de 285.82 ± 23.75 Ma (Westfaliense a Guadalupiense, incluyendo el margen de error el tránsito Carbonífero–Pérmico) y 246.87 ± 5.36 Ma (Triásico temprano), respectivamente. Se considera que las Cadenas Ibéricas representan la prolongación sudoriental de las zonas Cantábrica y Asturoccidental Leonesa del macizo Ibérico. La isograda varisca reconocida en las Cadenas Ibéricas representa la prolongación de las isogradas contemporáneas reconocidas en el extremo nororiental de la Sierra de la Demanda y el cinturón de Novellana-Pola de Allande-Degaña de la Zona Asturoccidental Leonesa. Esta distribución permite identificar un cinturón de metamorfismo sincinemático, a lo largo de una orientación actual NO-SE, a través del Antiforme del Narcea, el cabalgamiento de Anguiano y los cabalgamientos de Daroca, Jarque y Datos. Considerando los estilos de deformación y los grados de metamorfismo variscos, el cabalgamiento de Datos representa la prolongación del contacto que separa las zonas Cantábrica y Asturoccidental Leonesa en las Cadenas Ibéricas.

Palabras clave Biotita · Porfiroblasto · Isograda · Metasomatismo · Gondwana

1 Introduction

The Variscan Orogen developed as a result of the collision between already amalgamated Laurussia and Gondwana, during closure of the Palaeozoic Rheic Ocean (e.g., Martínez Catalán et al. 2007; Nance and Linnemann 2009; von Raumer and Stampfli 2008; Nance et al. 2012). In the Iberian Massif (Fig. 1a), the Cantabrian Zone represents an easterly directed foreland thrust and fold belt. Its Palaeozoic succession was deformed by a set of imbricate thrusts and coeval folds, and by late high-angle faults. The thin-skinned general structural pattern (Pérez-Estaún et al. 1988) is dominated by a principal décollement located within the Cambrian Láncara Formation, but complicated by the existence of other detachment levels (Julivert et al. 1968). Deformation within the main body of thrust slices took place at shallow crustal levels and, in general, involved neither foliations nor metamorphism. The latter reached the transition from anchimetamorphism to low-grade metamorphism in the (westernmost) inner thrust units, as suggested by the presence of syntectonic quartz-albite-muscovite-chloritoid/chlorite assemblages. Likewise, changes in the illite crystallinity occur, as it has been observed in some areas in which there is a thermal gradient increase related to nappe emplacement (Suárez et al. 1990). In contrast, the Variscan structure of the neighbouring West Asturian-Leonese Zone is characterized by widespread thick-skinned geometries, associated with fold nappes, ductile thrusts and foliations. They were formed as a result of three principal deformation phases, broadly coeval with various stages of regional metamorphism and syn- and post-tectonic granitoid intrusions. Broadly, the intensity of deformation and metamorphism increases from east (the foreland Cantabrian Zone) to west (the internal zone of the Variscan Orogen; Ábalos et al. 2002 and references therein).

Carls (1983), based on stratigraphic and facies similarities of Palaeozoic successions, suggested the Iberian Chains (then subdivided into the Badules and Herrera tectonostratigraphic units, separated by the Datos Thrust) could be considered as a lateral prolongation of the West Asturian-Leonese Zone. The author correlated the Cantabrian and Ebro Land areas (now known as the Cantabro-Ebroan Land of the West African craton; Aramburu et al. 1992; Álvaro et al. 2003) as a common siliciclastic source in West Gondwana and considered the Azuara Block (an inlier placed to the east of the Datos Thrust) as a putative prolongation of the Cantabrian Zone.

Subsequently, Gozalo and Liñán (1988) proposed the subdivision of the Variscan basement into the Badules, Mesones and Herrera tectonostratigraphic units (separated by the Jarque and Datos Thrusts; Fig. 1b) and structurally correlated two Cadomian basements: the Narcea Antiform of NW Spain and the Paracuellos Antiform of the eastern Iberian Chain (Gutiérrez Alonso 2004; Álvaro et al. 2008) (Fig. 1a). The Jarque Thrust, which longitudinally crosscut the Paracuellos Antiform was then suggested as the prolongation of the contact between the Cantabrian and West Asturian-Leonese zones.

The construction of a high-speed train line and associated tunnels through the Paracuellos Antiform yielded a new structural model (Álvaro and Blanc-Valleron 2002). The antiform is a complex structure, represented by a broad anticline limited by two prominent tectonic structures: (1) the eastern Datos Thrust (or Nigüella-Monforte Fault *sensu* Casas et al. 2016) that flanks the Triassic Morés Trough; and (2) the western Embid Fault (Fig. 1b), marked in seismic profiles as a thin NE-dipping reflector. The Paracuellos Antiform is bounded to the west by several thrust systems that do not affect the cratonic basement on which the sedimentary prism was transported.

In the Iberian Chains, the youngest rocks pre-dating the Variscan orogeny are Namurian and earliest Westphalian in age (Sächer 1966; Villena and Pardo 1983). According to Villa et al. (1996, and references therein) and Carls et al. (2004, and references therein), the Upper Namurian–to–Westphalian (~325–308 Ma) Culm facies sedimentation represents the south-to-north progradation of a syn-orogenic depositional trough. In the neighbouring Demanda Massif, the Variscan deformation is relatively well-constrained, and the oldest post-tectonic rocks are Westphalian B–D strata that unconformably overlie folded and thrusted Palaeozoic rocks (Colchen 1974).

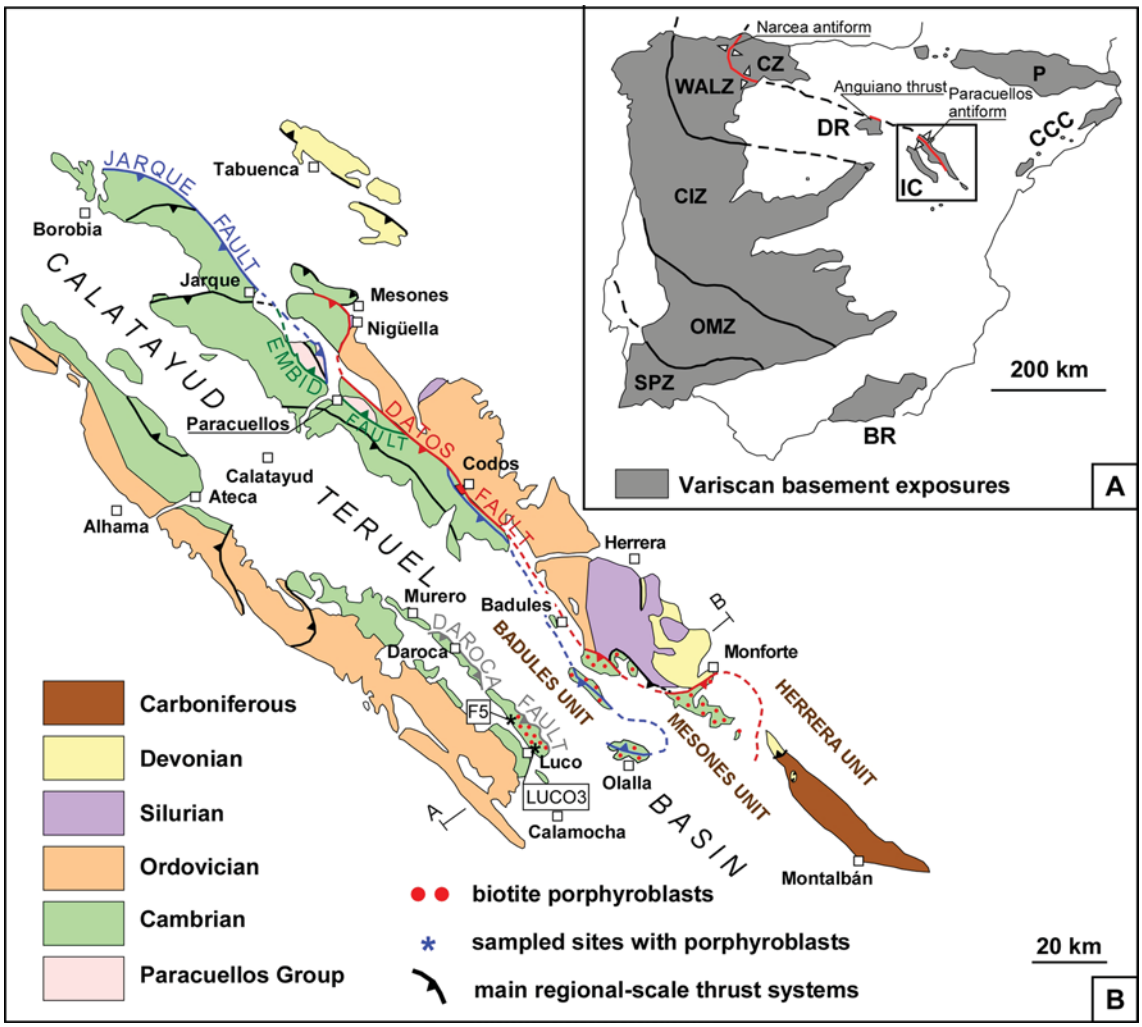

Fig. 1 **a** Variscan basement exposures in the Iberian Peninsula with Variscan subdivision into zones of the Iberian massif; modified from Julivert et al. (1972), Carls (1983) and Gozalo and Liñán (1988). *BR* Betic Ranges, *CCC* Coastal Catalonian Chain, *CIZ* Central Iberian Zone, *CZ* Cantabrian Zone, *DR* Demanda Ranges, *IC* Iberian Chains, *OMZ* Ossa-Morena Zone, *P* Pyrenees, *SPZ* South Portuguese Zone and WALZ West Asturian-Leonese Zone. **b** Geological sketch of Variscan basement exposures in the Iberian Chains, NE Spain; modified from Carls (1983) and Álvaro and Blanc-Valleron (2002)

Cambrian slates and marble successions contain metamorphic and hydrothermal biotite suites (e.g., Álvaro and Vennin, 1998) that could help shed light on the timing of Variscan deformation in the Iberian Chains. The aims of this paper are (1) to improve age constraints on Variscan deformation and post–Variscan thermal history in the Iberian Chains on the basis of detailed microstructural and petrographic analyses, geochemical data, and ^{40}Ar–^{39}Ar geochronology on biotite pophyroblasts and veinlet infills; and (2) to strengthen the longitudinal subdivision of the Iberian Chains into two main belts representing the lateral prolongation of the Cantabrian and West Asturian-Leonese Zones.

2 Geological setting and distribution of biotite porphyroblast-bearing rocks

In the Iberian Chains, the Cadomian, Variscan and Alpine structural trends are broadly subparallel (e.g., Capote and González Lodeiro 1983; Tejero and Capote 1987). As a result, these massifs contain the record of three orogenies whose effects are sometimes difficult to separate, except along Palaeozoic/post–Palaeozoic contacts (Liesa and Casas Sáinz 1994; Álvaro et al. 2008). The Variscan structures of the Iberian Chains are attributable to, at least, three major deformation phases (Capote and González Lodeiro 1983; Tejero and Capote 1987), which were developed under low to very low grade metamorphism (Navas and Tena 1988; Aparicio et al. 1991a, b; Mandado and Tena 1991; Bauluz

et al. 1998). A late Variscan deformation regime reflects an evolution from reverse strike-slip tectonics to radial extension (Tejero and de Vicente 1987) associated with Stephanian–Permian calc-alkaline dike and sill emplacement (Lago et al. 2004; Sanz et al. 2013). Finally, Alpine regional stress regimes affected pre-existing crustal discontinuities, reactivating both Variscan structures and discordant contacts of pre–Variscan lithological units with Triassic (Morés Trough) and Cenozoic (Calatayud-Teruel Basin) rocks (Julivert 1954; Colomer and Santanach 1988; Álvaro et al. 1992; Álvaro 1998) (Fig. 1b).

The eastern and western Iberian Chains constitute two parallel NW–SE alignments of structures generated during the superposition of the Variscan and Alpine orogenies and separated by the Neogene Calatayud-Teruel Basin. Major detachment levels are recognized in the shales of the Ediacaran–basal Cambrian Paracuellos Group and the Silurian Bádenas Formation (Álvaro et al. 2008; Calvín-Ballester and Casas 2013).

The Datos and Jarque thrusts are first-order structures, with NW–SE trends and NE vergences, which crosscut longitudinally the eastern Iberian Chain and separate it into three tectonostratigraphic units. These are known, from SW to NE, as the Badules, Mesones and Herrera units (Carls 1983; Gozalo and Liñán 1988). The Ediacaran–basal Cambrian Paracuellos Group forms the core of two disconnected antiform structures: the Paracuellos and Codos antiforms. Surface maps, seismic exploration data (acquired along a 5 km profile) and extensive drilling through the Paracuellos axial core allowed the recognition of two major NE-dipping basement faults, which could become listric at depth in a zone of lower crustal reflectivity. These major faults are subsequently affected by transcurrent shearing faults, observed on surface and interpreted as a result of a late Variscan phase of deformation (Álvaro and Blanc-Valleron 2002).

The Badules and Mesones units exhibit a common style of deformation. Their Ediacaran–to–Lower Ordovician rocks occur as a succession of imbricated SW-dipping thrust systems (Pérez-Lorente 1990; Navarro Vázquez 1991), bounded to the NE by NE-dipping basement faults associated with the Paracuellos antiform (Álvaro and Blanc-Valleron 2002). This thrust-and-nappe network was subsequently reactivated during the Alpine orogeny, as illustrated by Cambrian rocks thrusting on Triassic (Datos Thrust/Morés trough contact; Álvaro and Blanc-Valleron 2002) and Neogene (e.g., Daroca Thrust/Calatayud-Teruel Basin contact; Julivert 1954) troughs. In contrast, the Herrera Unit, which contains Cambrian to Carboniferous rocks, has been traditionally considered as formed by polyphase deformation characterized by a set of kilometre-scale, east-verging folds later affected by the east-directed thrust system associated with the Datos Thrust (Tejero and Capote 1987; Casas Sainz and Corés Gracia 1996).

In the southeastern edge of the eastern Iberian Chain, Calvín-Ballester and Casas (2013) reported the presence of two major Variscan deformation phases. D1 structures are related to the formation of thrust systems and subsidiary folding. Folds (F1) and associated cleavage (S_1) formed simultaneously during the emplacement of the successive sheets related to this thrust system. The emplacement of underlying thrust sheets resulted in progressive tilting and stacking, thus generating a foreland-dipping thrust system. D2 structures are mainly concentrated close to the Datos Thrust, showing steep dips and orientations consistent with large-scale eastward-verging folds, in agreement with the major structure. The intensity of deformation decreases with the distance to this fault. The Datos Thrust is also folded for this stage, indicating an early origin of this structure within D2. The latter kinematic model contrasts with the former one (Capote and González Lodeiro 1983; Tejero and Capote 1987), in which three main deformation phases were considered.

Biotite porphyroblasts and veinlet infills are hosted in the Cambrian slates and marble interbeds of the Ribota and Huérmeda formations and the overlying Cambrian Mesones and Acón groups. Their occurrence in the southeasternmost edge of both Chains (or inliers) was reported by Lotze (1929) and Lendínez González et al. (1989) in the eastern Iberian Chain, and by Álvaro (1998) and Álvaro and Vennin (1998) in the western Iberian Chain. Both transects consist of thin and elongated, NW–SE-trending belts, which correspond to the hanging walls of the Daroca, Jarque and Datos thrusts (Fig. 1b).

3 Materials and methods

Ten samples were characterized based on petrological, geochemical and structural data, two of which were dated geochronologically (Ferreruela and Luco de Jiloca; Figs. 1b, 2). Cambrian slates from the Ribota, Huérmeda and Valdemiedes formations were sampled at the hanging-wall of the Datos Thrust (site F5 from the Valdemiedes Formation; we differentiate a hydrothermal vein sample in this site as F5A—collected from the centre of the vein—and the host rock as F5). Cambrian slates and marbles of the Mesones Group were sampled at the hanging wall of the Daroca Thrust (LUCO-3 slate from the Valdemiedes Formation).

Polished thin sections were prepared at the 'Servicio de Apoyo a la Investigación' (SAI), University of Zaragoza, for petrological and geochemical examination using optical and scanning electron (SEM) microscopes and electron microprobe. SEM observations were performed at SAI with a Jeol JSM 6400 SEM equipped with an Oxford instrument detector (EDS) and using back-scattered electron (BSE) imaging and energy-dispersive X-ray (EDS) analysis to obtain

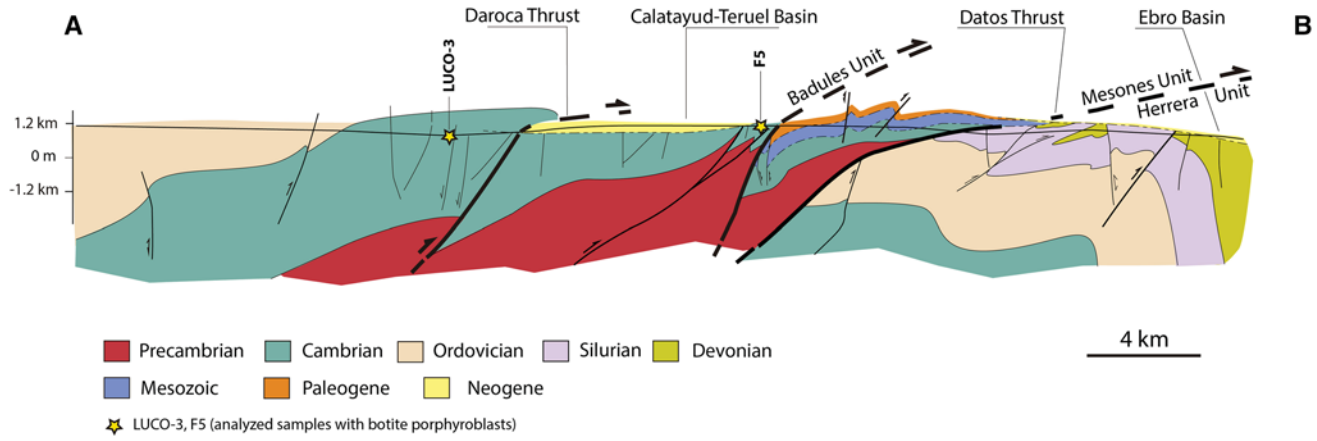

Fig. 2 Synthetic cross-section of the Iberian Chains through the study area with location of study samples; after Martín Fernández et al. (1977), Hernández Samaniego et al. (1980a, b) and Ruiz Fernández and Carls (1985). See location of trace in previous figure

textural and chemical information. Biotite crystals were analyzed by electron microprobe using a Cameca SX-50 at the Centres Científics i Tecnològics (University of Barcelona) with 20 kV voltage and beam current of 10nÅ for Fe, Mn, Ti, K, Ca, Mg, Na, Si, Al and 20nÅ for Ni, Cr, Ba, V, F, Rb. The detection limit was ±100 ppm. The standards used were fluorite (F), albite (Na), periclase (Mg), Al_2O_3 (Al), diopside (Si), orthoclase (K), wollastonite (Ca), rutile (Ti), vanadium (V), Cr_2O_3 (Cr), rhodonite (Mn), Fe_2O_3 (Fe), NiO (Ni), RTP (Rb) and barite (Ba).

The structural study included geometrical characterization of the main mesoscale ductile structures, as well as a detailed microstructural analysis on thin sections, including analysis of biotite porphyroblast/matrix relationships. This made it possible to establish the growth sequence of biotite crystals and their relationship with deformation.

Concerning the geochronological determinations, they were carried out using $^{40}Ar/^{39}Ar$ analysis on separated biotite porphyroblasts in slates (sample LUCO3, vein-free slate) and biotite infills from veins (sample F5A, centre of a vein, up to 2.5 cm long). Biotite separation was undertaken at the mineral separation laboratory of the VU University, Amsterdam. Samples were crushed and sieved to select the 150–300 µm size fraction for metamorphic biotite in LUCO3 and the 300–500 µm size fraction for the larger veinlet crystals in F5A. After cleaning with deionised water, biotite grains were separated using heavy liquids (LOC-50 Liquid Overflow Centrifuge model-50; IJlst 1973) and the Frantz® magnetometer. Biotite separates were finally purified by hand-picking and cleaned in an ultrasonic bath with deionised water. About 30 mg of each biotite separate were wrapped in an 8 mm diameter Al-foil package for irradiation. Sample packages and 8-10 mg aliquots of laboratory standard sanidine TCR-2 (25.42 Ma, calibrated following Kuiper et al. 2008) wrapped in Cu-foil were sealed in a 9 mm diameter ID quartz vial, with one standard package loaded at the top and bottom positions and between every 4 sample packages. The quartz vial was sealed in a standard Al-irradiation-capsule and irradiated for 12 h at HFR Petten (The Netherlands), operated by NRG, in the pool-side facility RODEO (rotating with a frequency of 1 Hz), fitted with a Cd tube to minimize the thermal neutron flux. Multigrain samples of irradiated biotite were loaded in Cu-discs and step-heated following the procedure described in Ubide et al. (2014). System blanks were run after every 3 or 4 steps and mass discrimination (1.034) was controlled by frequent analysis of $^{40}Ar/^{36}Ar$ air pipette aliquots.

4 Petro-structural constraints

Two biotite assemblages were recognized based on their crosscutting relationships with main cleavage planes (Figs. 4, 5). They are referred to as early porphyroblasts (metamorphic biotite; e.g., LUCO3) and late veinlet-infilling biotites (hydrothermal biotite; e.g., F5A). The early biotite porphyroblasts, usually larger than 50 µm, and typically 150–300 µm in size, occur as euhedral to subhedral crystals with abundant inclusions, mainly of quartz (Fig. 5a). The late biotites occur as anhedral crystals in the form of micron-sized patches or flakes of larger size (300–500 µm), along veinlets (Fig. 5b). The rock matrix is rich in chlorite, muscovite, quartz, K-feldspar and plagioclase (Fig. 5c, d).

4.1 Meso- and microscopic-scale tectonic analysis

At outcrop scale, the Cambrian rocks (mainly shales and sandstones) are affected by a conspicuous and penetrative slaty cleavage (S_{1N}), commonly subparallel to bedding (Fig. 3a, b). In the coarsest grained rocks, a common

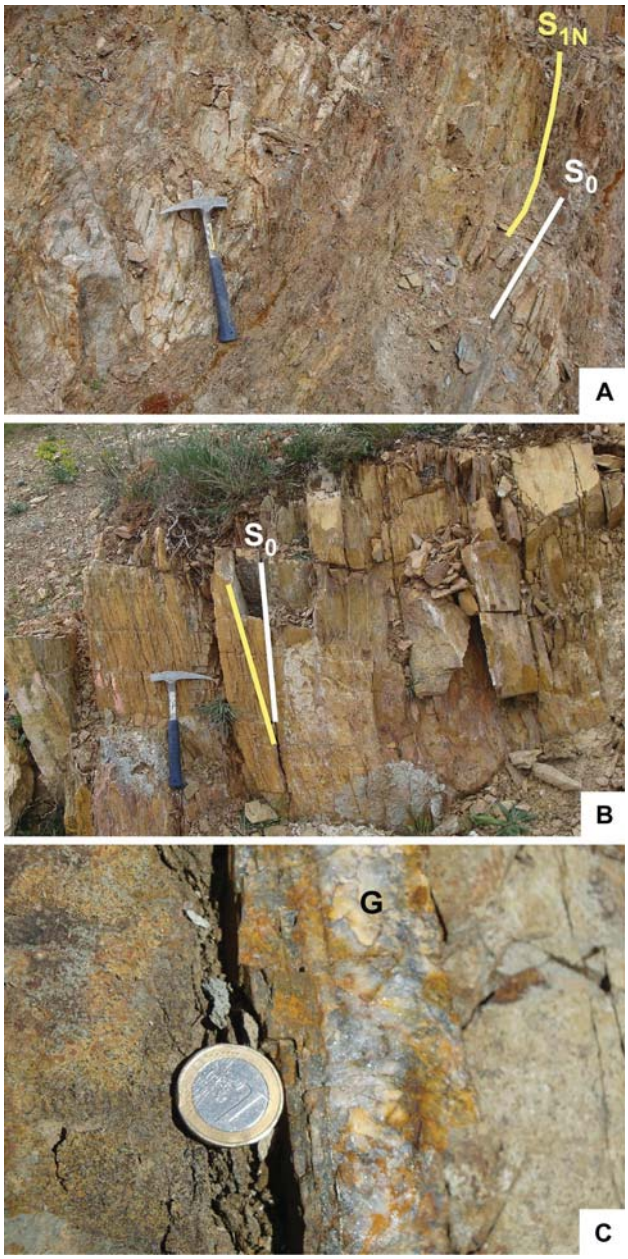

Fig. 3 Field context of biotite occurrences. **a**, **b** Cambrian shales with well-developed slaty cleavage (S_{1N}) subparallel to bedding (S_0); sites ANE and F5, respectively. **c** Detail of a centimetre-scale quartz tension gash (G) crosscutting a Cambrian siltstone

feature is the presence of centimetre- to decimetre-scale quartz tension gashes (Fig. 3c). At microscopic scale, the main cleavage (S_{1N}) is defined by preferred orientation of both lepidoblastic phyllosilicates and biotite porphyroblasts (LUCO3; Fig. 4a). However, a discontinuous and asymmetric crenulation cleavage (S_{2N}) commonly affects both S_{1N} and some of the most euhedral biotite porphyroblasts (F5; Fig. 4b, c).

The studied rocks classify as schists with biotite porphyroblasts encased in a recrystallized matrix, mainly composed of chlorite, muscovite and quartz, and subsidiary K-feldspar and plagioclase. Some other cleavaged clastic rocks include shales. In all the analysed cases, biotite crystals can be ascribed to one of two populations:

1. Euhedral to subhedral biotites occur mimetically oriented with respect to S_1 cleavage (syntectonic or early biotites). Such biotites consist of porphyroblasts with straight margins and exhibit large dimensions parallel with respect to cleavage S_1 (syntectonic). The fact that these biotites include cleavage S_{1N} demonstrates that these crystals grew relatively late with respect to the main deformation phase (D_{1N}). Early biotites also exhibit strain shadows of quartz in the direction of cleavage S_{1N} (F5; Fig. 4b, d), indicating that the last part of deformation D_{1N} postdated the growth of biotite porphyroblasts. In some cases, the early euhedral porphyroblasts are also affected by D_{2N} (Fig. 4c).
2. A second group of randomly oriented biotite crystals is represented by anhedral veinlet-occluding crystals, which include the asymmetrical crenulation cleavage S_{2N}. This indicates that the growth of late biotites postdated deformation D_{2N} (Fig. 4b). These late anhedral biotite crystals are both closely linked to brittle deformation, inferred from their high abundance within quartz tension gashes, and scattered in the rock-matrix (site F5A in Fig. 4c and site F5A in Fig. 4e). Such quartz veinlets crosscut foliation S_{1N} and, in some cases, are subparallel to S_{2N}; this relationship suggests that both structures (veinlets and S_{2N}) are not cinematically compatible (F5A in Fig. 4e, f).

Based on this microtectonic analysis, the population of early euhedral (metamorphic) biotite porphyroblasts is considered as syntectonic respect to the main deformation phase (D_{1N}), whereas the late anhedral veinlet biotite crystals postdate the deformation phase D_{2N}.

4.2 Biotite chemistry

Back Scattered Electron (BSE/SEM) images indicate that the early porphyroblasts and the late veinlet crystals share homogeneous compositions (Table 1; Fig. 5). The matrix plagioclase has average compositions of $Ab_{50}An_{50}$ according to SEM/EDS analyses. A total of 59 electron-microprobe biotite analyses were obtained from early and late porhyroblasts. Analyses correspond to K-rich trioctahedral micas (Table 1) with 2.86 atoms per formula unit (apfu) in the octahedral sheet, K as major cation in the interlayer sites (0.80 apfu), and a Fe/Fe + Mg ratio of 0.54. The plotting of these data in

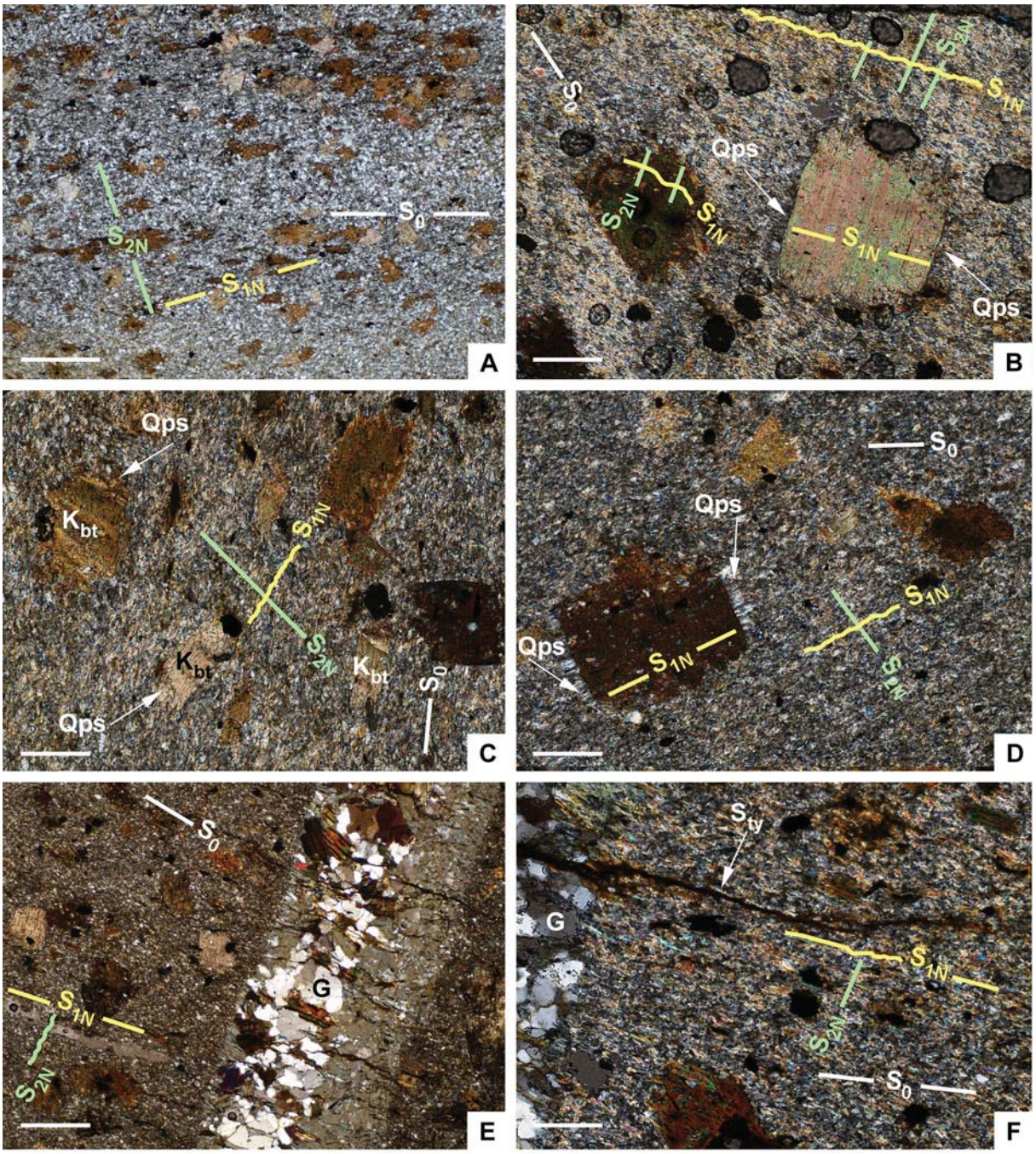

Fig. 4 Photomicrographs of metamorphic paragenesis in the Cambrian shales of the Valdemiedes Formation. **a** Slaty cleavage S_{1N} in a micaschist affected by a discontinuous asymmetric crenulation cleavage S_{2N} (site LUCO3); note the preferred orientation of biotite porphyroblasts; scale-bar = 500 µm. **b–d**. Textural relationships of the two populations of biotite porphyroblasts hosted by deformed silty micaschists; note the quartz strain shadows (Q_{PS}), compatible with cleavage S_{1N} and the crenulation (kinking) of the most euhedral porphyroblasts (K_{Bt} compatible with cleavage S_{2N}), and the most xenomorphic crystals including cleavage S_{2N} (**b** from LUCO3, and **c**, **d** from F5); scales-bars = 200 µm. **e**, **f** Details of tension gashes (G) affecting cleavages S_{1N} and S_{2N} (site F5A); note the extremely high concentration of anhedral biotites within them. In all the cases, S_0 indicates bedding trace; scales-bars = 500 and 200 µm, respectively. See text for details

the trioctahedral mica quadrilateral of Guidotti (1984) shows that the biotite compositions are closer to the eastonite and siderophyllite fields than to the phlogopite and annite fields (Fig. 6). In the classification diagram of Tischendorf et al. (1997), the chemical compositions of the analyzed biotites plot in the limit between Mg-biotite and Fe-biotite.

Table 1 Chemical composition of analysed biotites; formula of biotites based on 11 oxygens and trace elements in ppm; F/FM = Fe/Fe + Mg, Soct = Sum of octahedral cations, Int. Ch. = Interlayer charge

	Biotite porphyroblasts																			
	Si	AlIV	AlVI	Ti	Fe	V	Mn	Mg	Soct	F/F+M	Ca	Na	K	Rb	Int. Ch.	F (ppm)	V (ppm)	Cr (ppm)	Mn (ppm)	Ni (ppm)
F5-A-1-1	2.76	1.24	0.47	0.09	1.25	0.01	0.01	1.01	2.85	0.55	0.01	0.02	0.82	0.00	0.86	4193	865	228	1402	0
F5-A-1-3	2.75	1.25	0.43	0.09	1.28	0.01	0.01	1.07	2.89	0.54	0.01	0.02	0.80	0.00	0.84	4388	887	214	933	132
F5-A-1-4	2.76	1.24	0.46	0.09	1.24	0.01	0.01	1.07	2.88	0.54	0.01	0.02	0.79	0.01	0.84	5183	862	197	1211	146
F5-A-1-5	2.77	1.23	0.46	0.08	1.28	0.01	0.01	1.06	2.90	0.55	0.02	0.02	0.73	0.00	0.79	4598	742	153	1657	191
F5-A-1-10	2.76	1.24	0.45	0.09	1.22	0.01	0.01	1.09	2.86	0.53	0.00	0.01	0.85	0.00	0.87	5310	786	200		0
F5-A-1-11	2.74	1.26	0.42	0.10	1.30	0.01	0.01	1.05	2.89	0.55	0.00	0.01	0.82	0.00	0.85	4663	865	168	1276	0
F5-A-2-1	2.79	1.21	0.47	0.08	1.20	0.01	0.01	1.09	2.87	0.52	0.02	0.02	0.76	0.01	0.82	4482	788	192	1597	171
F5-A-2-2	2.79	1.21	0.47	0.09	1.13	0.01	0.01	1.13	2.84	0.50	0.01	0.02	0.81	0.01	0.86	4973	850	214	957	137
F5-A-2-3	2.76	1.24	0.47	0.09	1.18	0.01	0.01	1.09	2.86	0.52	0.01	0.02	0.81	0.01	0.85	7448	837	214	1605	130
F5-A-2-4	2.78	1.22	0.45	0.09	1.21	0.01	0.01	1.08	2.85	0.53	0.04	0.02	0.76	0.01	0.85	3929	952	294	1589	142
F5-A-4-2	2.77	1.23	0.46	0.09	1.25	0.01	0.01	1.04	2.86	0.55	0.01	0.02	0.81	0.01	0.86	5352	799	206	1167	149
F5-A-4-3	2.74	1.26	0.40	0.09	1.32	0.01	0.01	1.08	2.91	0.55	0.01	0.02	0.81	0.00	0.85	3430	805	201	1207	75
F5-A-7-7	2.77	1.23	0.47	0.09	1.17	0.01	0.01	1.09	2.85	0.52	0.01	0.02	0.82	0.00	0.86	4901	965	243	1782	0
F5-A-7-8	2.75	1.25	0.43	0.09	1.24	0.01	0.01	1.09	2.88	0.53	0.01	0.02	0.81	0.00	0.86	3906	953	207	0	0
F5-A-7-9	2.75	1.25	0.50	0.09	1.17	0.01	0.01	1.07	2.84	0.52	0.00	0.02	0.84	0.00	0.86	4619	934	229	1011	165
F5-A-7-10	2.80	1.20	0.48	0.10	1.15	0.01	0.01	1.07	2.82	0.52	0.01	0.02	0.83	0.01	0.87	4917	929	258	0	109
F5-A-7-11	2.78	1.22	0.47	0.09	1.20	0.01	0.01	1.07	2.86	0.53	0.02	0.01	0.77	0.01	0.83	5271	948	256	1440	237
F5-A-7-12	2.76	1.24	0.49	0.09	1.20	0.01	0.02	1.06	2.87	0.53	0.02	0.02	0.75	0.01	0.81	1913	826	245	1842	0
F5-A-7-13	2.76	1.24	0.62	0.07	1.13	0.01	0.01	0.96	2.80	0.54	0.02	0.02	0.79	0.00	0.85	3731	680	264	1506	0
F5-A-7-14	2.73	1.27	0.44	0.09	1.24	0.01	0.01	1.09	2.88	0.53	0.01	0.02	0.83	0.00	0.87	4296	839	204	1367	0
F5-A-7-15	2.78	1.22	0.45	0.09	1.20	0.01	0.01	1.10	2.86	0.52	0.02	0.02	0.80	0.01	0.86	4823	833	193	1504	169
F5-A-7-16	2.74	1.26	0.47	0.09	1.20	0.01	0.01	1.10	2.88	0.52	0.00	0.02	0.80	0.01	0.83	2974	821	179	974	0
F5-A-7-17	2.75	1.25	0.46	0.10	1.24	0.01	0.01	1.04	2.85	0.54	0.00	0.02	0.82	0.00	0.86	3249	943	243	0	179
F5-A-1-6	2.81	1.19	0.69	0.08	1.08	0.01	0.01	0.87	2.73	0.56	0.01	0.03	0.81	0.00	0.86	3085	761	241	1362	186
F5-A-1-7	2.75	1.25	0.47	0.12	1.25	0.01	0.01	0.98	2.84	0.56	0.01	0.02	0.82	0.00	0.85	2805	1016	235	1153	164
F5-A-1-8	2.98	1.02	0.55	0.09	1.15	0.01	0.01	0.94	2.75	0.55	0.01	0.02	0.74	0.01	0.79	5089	869	259	0	0
F5-A-1-9	2.76	1.24	0.46	0.10	1.25	0.01	0.01	1.04	2.86	0.55	0.01	0.01	0.80	0.00	0.83	5302	918	352	1147	0
F5-A-7-2	2.61	1.39	0.37	0.10	1.41	0.01	0.01	1.12	3.02	0.56	0.00	0.02	0.74	0.01	0.77	3490	1015	160	1580	172
F5-A-7-3	2.80	1.20	0.48	0.10	1.18	0.01	0.01	1.04	2.82	0.53	0.01	0.01	0.82	0.01	0.85	3616	882	182	858	0
F5-A-7-4	2.79	1.21	0.43	0.10	1.24	0.01	0.01	1.06	2.86	0.54	0.01	0.02	0.80	0.01	0.84	4308	885	183	1407	0
F5-A-7-5	2.74	1.26	0.41	0.09	1.34	0.01	0.02	1.02	2.89	0.57	0.03	0.02	0.78	0.00	0.85	4476	874	194	1798	0
F5-A-7-6	2.71	1.29	0.39	0.09	1.33	0.01	0.01	1.13	2.95	0.54	0.01	0.01	0.77	0.01	0.80	4620	906	265	878	0

Table 1 (continued)

	Si	AlIV	AlVI	Biotite veinlets Ti	Fe	V	Mn	Mg	Soct	F/F+M	ca	na	k	rb	int. ch.	f (ppm)	v (ppm)	Cr (ppm)	Mn (ppm)	Ni (ppm)
F5-A-3-1	2.79	1.21	0.47	0.09	1.20	0.01	0.01	1.07	2.86	0.53	0.03	0.02	0.73	0.00	0.81	5161	1030	249	1749	166
F5-A-3-4	2.82	1.18	0.44	0.10	1.24	0.01	0.01	1.06	2.86	0.54	0.02	0.02	0.74	0.00	0.80	4970	807	106	1369	0
F5-A-3-7	2.79	1.21	0.48	0.10	1.21	0.01	0.01	1.03	2.83	0.54	0.02	0.02	0.79	0.01	0.85	5049	882	199	942	193
F5-A-4-4	2.77	1.23	0.42	0.09	1.29	0.01	0.01	1.06	2.88	0.55	0.03	0.02	0.75	0.01	0.84	5153	701	36	1244	170
F5-A-4-6	2.76	1.24	0.48	0.09	1.23	0.01	0.01	1.04	2.85	0.54	0.04	0.02	0.75	0.00	0.86	3304	767	159	1456	156
F5-A-4-7	2.78	1.22	0.48	0.08	1.24	0.01	0.01	1.05	2.88	0.54	0.02	0.02	0.73	0.00	0.80	2846	731	–	1311	150
F5-A-4-9	2.78	1.22	0.44	0.10	1.26	0.01	0.00	1.05	2.86	0.54	0.01	0.02	0.80	0.01	0.85	3849	809	140	–	–
F5-A-5-1	2.78	1.22	0.48	0.08	1.22	0.01	0.01	1.06	2.86	0.53	0.01	0.01	0.81	0.01	0.85	4469	630	164	–	292
F5-A-5-2	2.82	1.18	0.48	0.09	1.18	0.01	0.01	1.07	2.84	0.52	0.01	0.02	0.78	0.01	0.84	3322	666	212	1673	145
F5-A-5-5	2.78	1.22	0.46	0.09	1.25	0.01	0.01	1.06	2.88	0.54	0.01	0.01	0.77	0.01	0.81	2403	654	183	1548	178
F5-A-5-6	2.78	1.22	0.58	0.09	1.11	0.01	0.01	1.00	2.79	0.53	0.01	0.02	0.82	0.01	0.87	2674	728	176	1197	0
F5-A-5-7	2.79	1.21	0.45	0.09	1.22	0.01	0.01	1.10	2.86	0.53	0.03	0.02	0.77	0.01	0.85	3357	686	190	832	132
F5-A-5-8	2.78	1.22	0.48	0.09	1.19	0.01	0.01	1.08	2.84	0.52	0.02	0.02	0.79	0.01	0.86	2591	671	200	1024	153
F5-A-6-1	2.75	1.25	0.45	0.08	1.24	0.01	0.01	1.09	2.88	0.53	0.02	0.02	0.78	0.00	0.86	3736	633	125	1282	128
F5-A-6-2	2.76	1.24	0.47	0.09	1.30	0.01	0.02	1.00	2.88	0.56	0.01	0.02	0.79	0.00	0.82	3555	662	154	1756	144
F5-A-6-3	2.75	1.25	0.48	0.09	1.26	0.01	0.02	1.01	2.86	0.55	0.01	0.02	0.81	0.00	0.85	2573	740	146	1834	–
F5-A-6-4	2.78	1.22	0.48	0.09	1.21	0.01	0.01	1.07	2.86	0.53	0.02	0.02	0.76	0.00	0.83	4144	686	189	1095	126

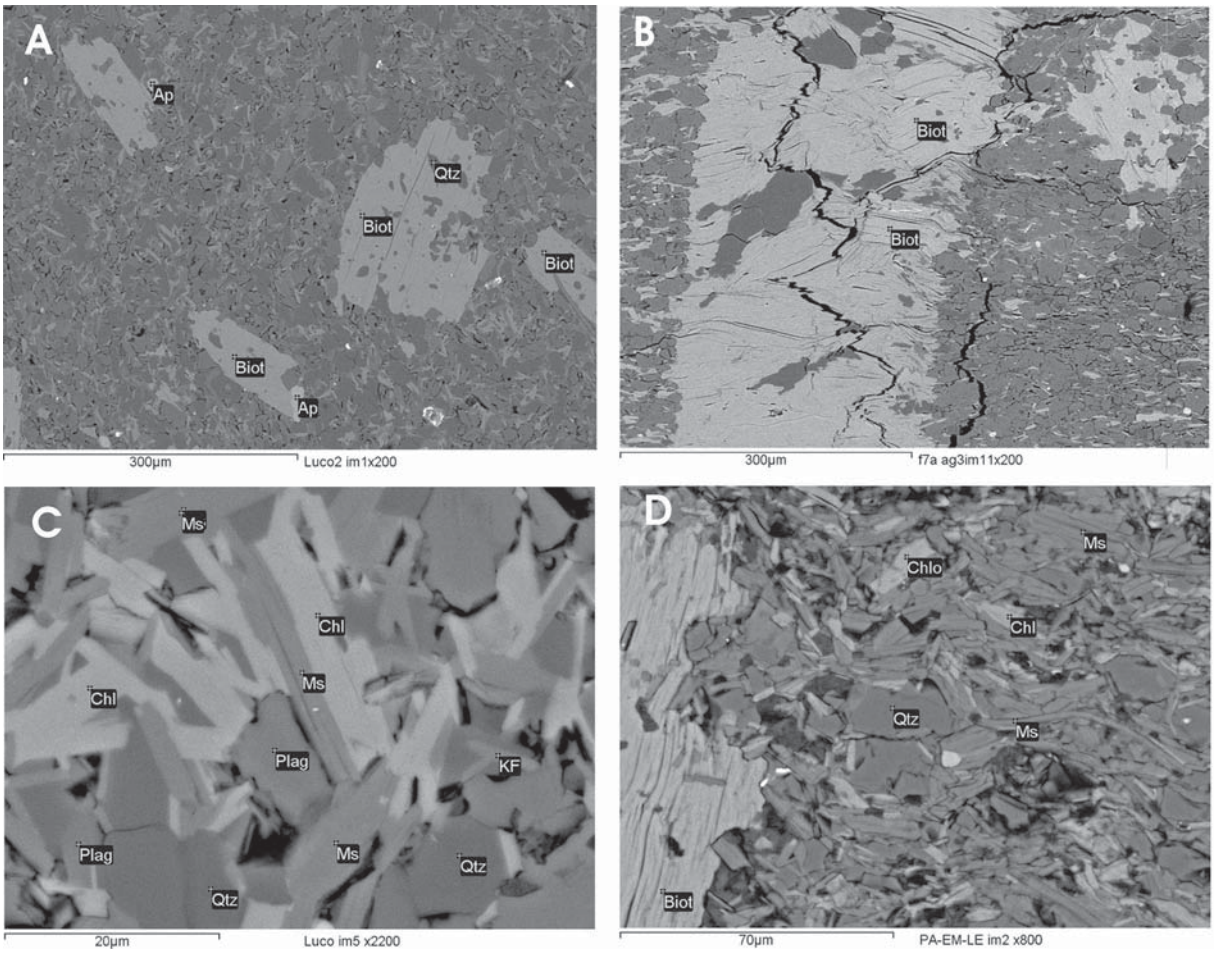

Fig. 5 Representative backscattered images (BSE/SEM) of analyzed samples. **a** Textural image showing porphyroblasts of biotite with mineral inclusions in a recrystallized matrix. **b** Biotites that grow occluding a fissure network. **c**, **d**. Images of recrystallized matrix. *Ap* apatite, *Biot* biotite, *Chl* chlorite, *KF* K-feldspar, *Ms* muscovite, *Plag* plagioclase, *Qtz* quartz

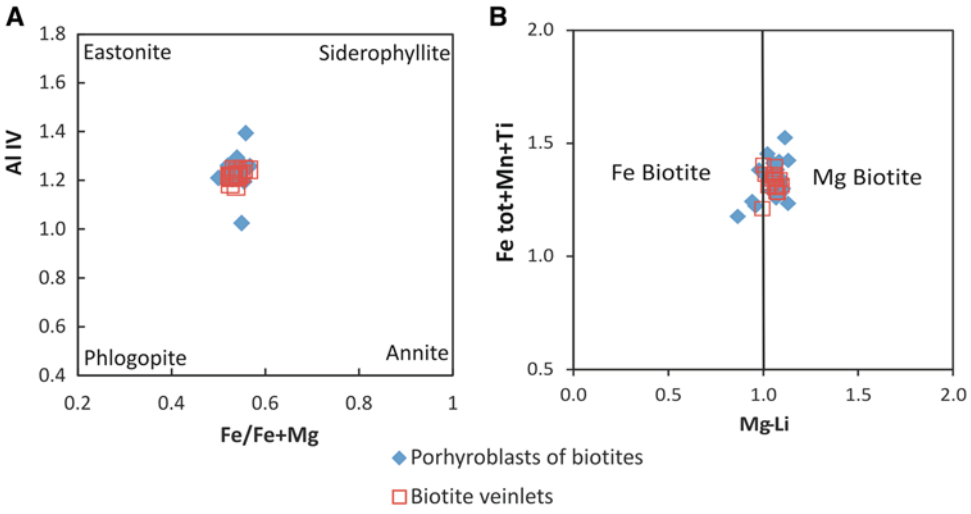

Fig. 6 Biotite compositions obtained by in situ major element analysis with electron microprobe. Compositions recalculated to cations per formula unit (on the basis of 11 oxygens). **a** Fe/Fe + Mg vs Al^{IV} graph showing the compositional homogeneity of early biotite porphyroblasts and late biotites from veinlets. **b** Fe_{tot}-Mn–Ti vs Mg–Li graph showing that the compositions plot in the boundary between Mg-biotite and Fe-biotite fields

The early porphyroblasts and the late veinlet crystals of biotite display similar compositions (Table 1), with identical averages both for major and minor elements. Overall, our data reflect that the biotites from veinlets have more homogeneous composition than the porphyroblasts, probably due to contamination related to inclusions in the porphyroblasts.

The chemistry of hydrothermal biotites depends on several factors, such as the temperature and composition of hydrothermal fluids (e.g., oxygen fugacity, and Mg–Fe^{2+}–Fe^{3+} proportions), but the temperature formation usually ranges from 300 to 400 °C (Beane 1974; Ayati et al. 2008).

4.3 $^{40}Ar/^{39}Ar$ geochronology

$^{40}Ar/^{39}Ar$ experiments on biotite separates yielded complicated age profiles, reflecting long and complex tectonothermal histories. $^{40}Ar/^{39}Ar$ results are summarised in Fig. 7 and Table 2, with uncertainties quoted at 2σ. Full data tables can be found in the electronic supplement.

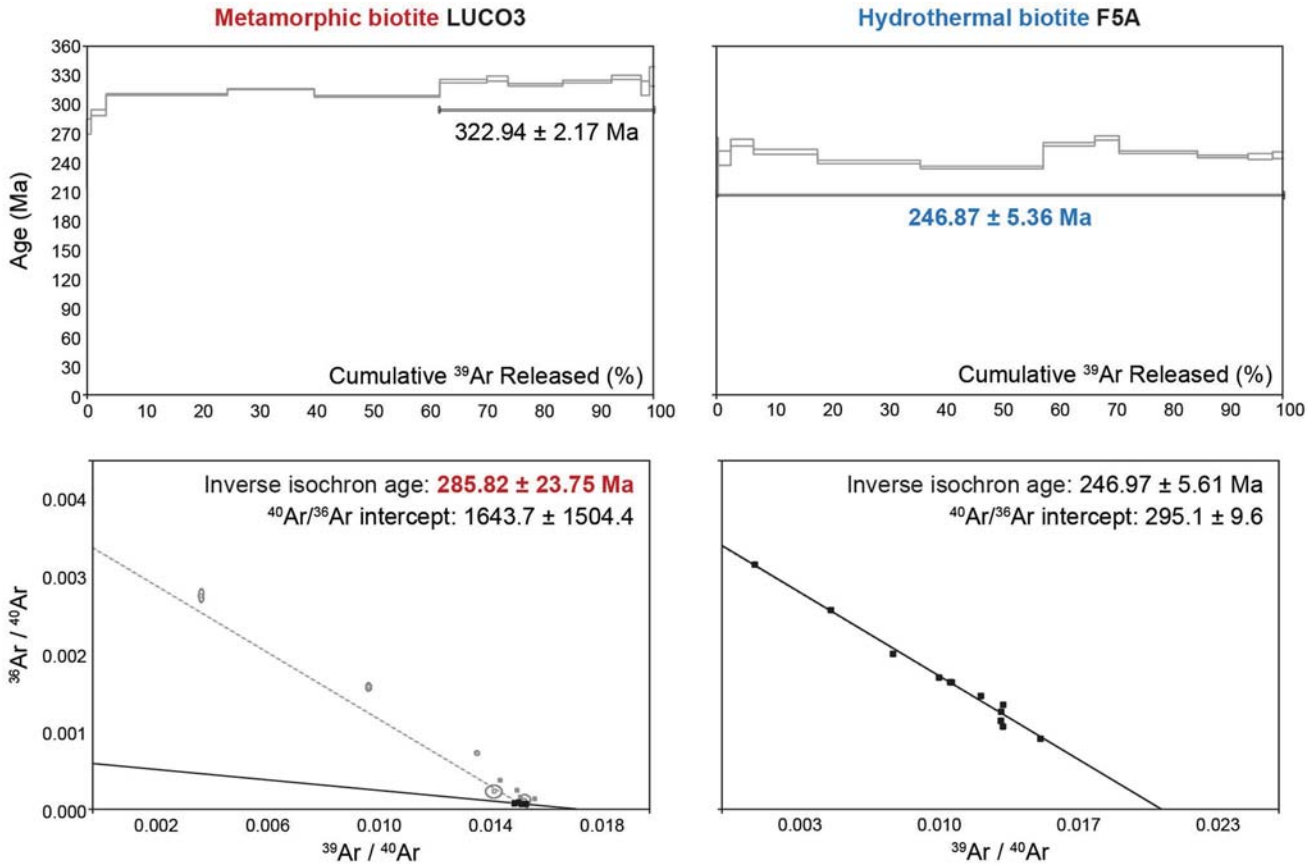

Fig. 7 $^{40}Ar/^{39}Ar$ incremental heating results for biotite separates from samples LUCO3 and F5A, presented in age spectra and inverse isochron plots. In the age spectra, the thickness of the steps reflects the associated uncertainty; the black horizontal line covers the age-defining steps. In the inverse isochron diagrams, the dashed line represents the ideal atmospheric-radiogenic mixing line, whereas the solid line represents the inverse isochron calculated with selected steps (black squares); square size includes uncertainty when not shown

Table 2 Summary of $^{40}Ar/^{39}Ar$ data; preferred ages are marked in bold

Sample	Separated phase	Type	Plateau age	±2σ	MSWD	%39Ar, n steps	Inverse isochron age	±2σ	MSWD	K/Ca	±2σ
LUCO3	Biotite	Metamorphic	322.94	±2.17	9.11	37.8	**285.82**	**±23.75**	**3.74**	0.09	±0.07
				±0.67%		7		**±8.31%**			
F5A	Biotite	Hydrothermal	**246.87**	**±5.36**	**88.76**	100.0	246.97	±5.61	>100	1.30	±0.48
				±2.17%		12		±2.27%			

Full data tables are available in electronic format

Sample LUCO3 (early biotite porphyroblasts) produced an increasing age pattern (Fig. 7) related to diffusion loss (McDougall and Harrison 1999). In such cases, the oldest recorded age is the best estimate of the original age before the diffusion event and the high temperature steps define an age of 322.94 ± 2.17 Ma (Lower Carboniferous). We note, however, that these steps represent less than 50% of the ^{39}Ar released (ca. 40%) and the age results should be considered with care. The ^{40}Ar/^{36}Ar intercept for the trapped argon derived from the inverse isochron treatment of the high temperature data is higher than the atmospheric ratio of 295.5, suggesting excess argon in the system (McDougall and Harrison 1999). The inverse isochron age should therefore be preferred over the plateau age (McDougall and Harrison 1999; Renne et al. 2009). Hence, we infer that the best estimate of the true crystallisation age may be 285.82 ± 23.75 Ma (Lower Permian) (Fig. 7).

Sample F5A (late veinlet biotite crystals) showed a broader scatter without reaching a partial plateau (as defined by McDougall and Harrison 1999) at any stage along the age profile. In this case, 100% of ^{39}Ar was considered to calculate a summary age over all steps of 246.87 ± 5.36 Ma (Lower Triassic). The high value for the Mean Squares of Weighted Deviates (MSWD; Table 2) reflects the scatter between the steps. However, this age is in agreement within error with the inverse isochron age (246.97 ± 5.61 Ma), which shows a good regression to atmosphere (Fig. 7). In this case, excess argon is not a major issue and the obtained age is likely a reasonable estimate of crystallisation age.

5 Discussion: tectonothermal evolution in the Iberian Chains

The southeastern prolongation of the Variscan, Cantabrian and West Asturian-Leonese zones has been an everlasting matter of debate (Carls 1983; Gozalo and Liñán 1988; Álvaro et al. 2008). The Cantabrian Zone displays a thin-skinned type of structural geometry, in which the basement was not involved in the deformation, complicated by the existence of several detachment levels. The deformation took place under shallow crustal conditions, with only local development of cleavage. Metamorphism reached the transition from anchizone to low grade in the innermost thrust units (Pérez-Estaún and Bastida 1990; García-López et al. 1997; Bastida et al. 1999).

In contrast, the West Asturian-Leonese Zone shows thick-skinned tectonics with involvement of at least a part of the basement. Three main cleavage-related deformation phases developed under metamorphic (essentially synkinematic) conditions. In the northwesternmost part of the West Asturian-Leonese Zone, the distribution of the dynamo-thermal metamorphic zones points to a westward increase in epi- to catazonal metamorphic conditions. Three successive metamorphic events may be distinguished: (1) a Barrovian-type event developed under a medium-pressure geothermal gradient, including staurolite and kyanite-bearing parageneses, (2) a low-pressure, high-temperature event, including andalusite and sillimanite-bearing parageneses, and (3) an event of retrograde character. The relationship between mineral crystallization and cleavage development changes from one zone to another (Martínez Catalán 1985; Martínez Catalán et al. 1990; Pérez-Estaún et al. 1991; García-López et al. 2007).

Low metamorphic conditions, similar to those reported in this work, occur in the vicinity of the Narcea Antiform and the Demanda Massif (Fig. 8). In the former, two main metamorphic parageneses may be differentiated in pelitic rocks (Aparicio et al. 1993; Ábalos et al. 2002; Gutiérrez-Alonso 2004). The easternmost Narcea Antiform is located within the chlorite zone, with a muscovite-chlorite-chloritoid paragenesis of crystals oriented defining the axial-planar tectonic foliation S_1 linked to deformation phase D1, Early Carboniferous in age (Pérez-Estaún 1978; Martínez et al. 1988; Dallmeyer et al. 1997). Chlorite porphyroblasts with their larger dimensions lying parallel to the original bedding are transverse or obliquely arranged to S_1 cleavage and show large pressure shadows within S1 cleavage, where S_0 and S_1 intersect at high angles. The most important episode of chlorite and muscovite crystallization is syntectonic, although, in some cases, it might be post-tectonic (Suárez et al. 1990). The second metamorphic unit is located in the Novellana-Pola de Allande-Degaña Belt, which partially overlaps the western limb of the Narcea Antiform. Biotite is the significant index mineral in the Neoproterozoic shales, which occurs both randomly arranged or mimetically with respect to cleavage S_1. Chlorite, muscovite and recrystallized quartz are also well developed. In the neighbouring Demanda Massif, considered as a lateral prolongation of the Western Asturian-Leonese Zone, the regional metamorphism gave rise to chlorite growth across wide areas (Colchen 1974; Aparicio et al. 1991a, b).

As reported above, despite the large dating error for the metamorphic peak (including the Carboniferous–Permian transition) and the main Variscan-related deformation event D_{1N} recorded in the Iberian Chains, the studied paragenesis fits well with the W-E-trending variation pattern of the metamorphic isograds, allowing a reasonable correlation between tectono-metamorphic conditions from the northwesternmost sector (Novellana-Pola de Allande-Degaña Belt of the West Asturian-Leonese Zone) to the southeasternmost one, within the Iberian Chains, following the Narcea Antiform, the Anguiano Thrust and the Daroca, Jarque and Datos thrusts. However, the eastward decrease in metamorphic grade across the Narcea Antiform and the Demanda Massif contrasts with the southeastern increase in metamorphic

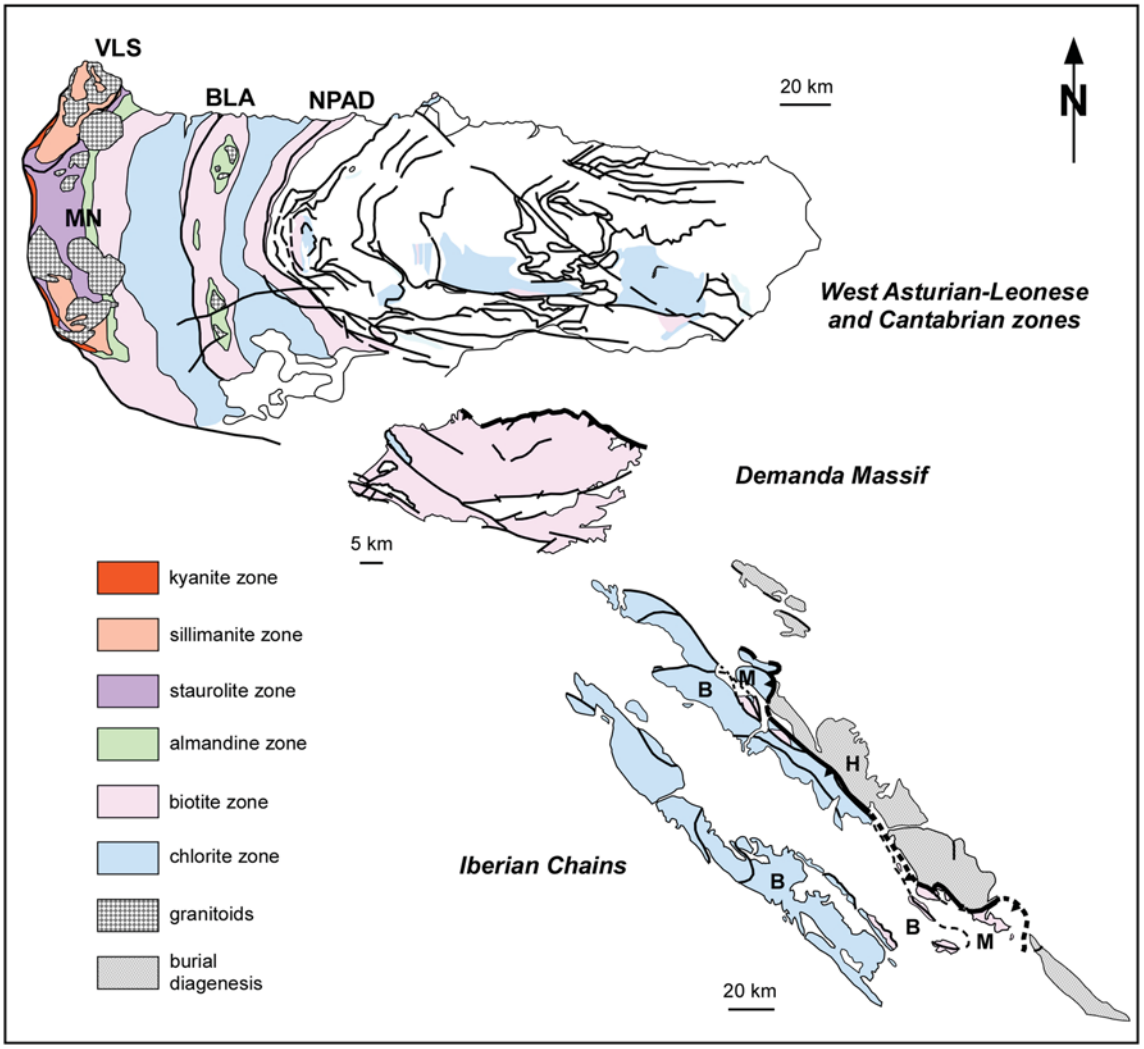

Fig. 8 Distribution of metamorphic belts in the Variscan basement of the West Asturian-Leonese and Cantabrian zones (A), the Demanda Massif (B) and the Iberian Chinas (C); based on Colchen (1974), Suárez et al. (1990), Aparicio et al. (1991a), Bauluz et al. (1998), Arenas and Martínez Catalán (2003), García-López et al. (2007), Álvaro et al. (2008) and this work; abbreviations of tectonostratigraphic units: *B* Badules, *BLA* Boal-Los Ancares, *H* Herrera, *M* Mesones, *NPAD* Novellana-Pola de Allande-Degaña and *VLS* Vivero-Lugo-Sarria

conditions (and occurrence of a biotite isograd in the hanging walls of the Daroca, Jarque and Datos thrusts) along the southeastern edges of the eastern and western Iberian Chains.

The tectonothermal evolution reported in inner parts of the Variscan foldbelt, represented by the Cantabrian and eastern part of the West Asturian-Leonese zones (a case study from the Mondoñedo nappe occurs in Arenas and Martínez Catalán 2003) (Fig. 8), and their southeastern prolongation into the Iberian Chains, differs from that recorded in external parts of the Variscan Orogen, such as the westernmost West Asturian-Leonese Zone and most of the northern Central-Iberian Zone of the Iberian Massif (Arenas and Martínez Catalán 2003; Rubio Pascual et al. 2013; Martínez Catalán et al. 2014, and references therein), the French Massif Central (Ledru et al. 2001), the Bohemian Massif (Schuevens 2002), the Variscan basement of the Pyrenees (Aerden 1994) and Sardinia (Casini and Oggiano 2008). Throughout the Central-Iberian Zone and the eastern branch of the Variscan Ibero-Armorican Arc (or external part of the Variscan foldbelt), late Variscan extension was commonly accompanied by HT-LP metamorphism related to anatexis and pluton emplacement. In contrast, the most thickened sections of the internal zones with metamorphic nappes (Cantabrian and West Asturian-Leonese zones and their lateral prolongation into the Demanda Massif and the Iberian Chains) underwent an important thermal increase, which can be directly linked to metamorphic isogrades.

Regarding the Late Permian extensional episode linked to the onset of the above-reported biotite veinlets (Tejero

and de Vicente 1987; López-Gómez et al. 2002), this event clearly post-date both (1) the early D_{1N} compressive deformation phase linked to the main regional foliation S_{1N}, and (2) the latter D_{2N} compressive deformation responsible for the record of the asymmetrical crenulation cleavage S_{2N}. Both foliations fit well with the Variscan tectonic scenario recognized for the Iberian Chains, where their first and second major deformation stages were associated with cleavage-related phases (Capote and González Lodeiro 1983; Tejero and Capote 1987).

6 Conclusions

Two successive biotite-rich parageneses, metamorphic and metasomatic in character, occur in Cambrian metapelites and marbles neighbouring the Daroca, Jarque and Datos thrusts of the Iberian Chains. They are geochemically similar but associated with different textures (porphyroblasts vs. veins). Based on a combination of microstructural analysis and $^{40}Ar/^{39}Ar$ geochronology, we provide improved constraints on the age of two Variscan deformation events: (1) a D_{1N} deformation event, related to high ductile deformation, ended with the crystallisation of metamorphic biotite porphyroblasts at latest Westphalian–to–Guadalupian times (285.82 ± 23.75 Ma); we note that the error is significant and related to diffusion loss of Ar; and (2) a later D_{2N} event responsible for an asymmetric and discontinuous crenulation cleavage, predating anhedral biotite growth (average age 247 ± 5 Ma). The latter hydrothermal event is compatible with the extensional tectonic framework characterizing the onset of the Apine Cycle in the Iberian Chains.

The southeastern prolongation of the Variscan, Cantabrian/West Asturian-Leonese zones contact is recognized along the Datos Thrust, a major structural accident that subdivides longitudinally the eastern Iberian Chain. To the NE of this contact, the Variscan orogeny is characterized by thin-skinned geometries where deformation took place under shallow crustal conditions, involving anchimetamorphism and local development of cleavage. In contrast, to the SW of the Datos Thrust, deformation took place under different metamorphic conditions. The reported tectono-thermal pattern is characterized by a heterogeneous distribution of metamorphic facies, with an essentially synkinematic chlorite + biotite + plagioclase paragenesis and well-developed cleavage-related biotite porphyroblasts linked to the main Variscan tectonic structures. The metamorphic distribution emphasized along the hanging walls of the Daroca, Jarque and Datos thrusts fits well with the metamorphic isograde recorded in the Novellana-Pola de Allande-Degaña Belt of the West Asturian-Leonese Zone and the Anguiano Thrust of the Demanda Sierra. Based on structural and metamorphic features, the Datos Thrust represents the contact that separates the Cantabrian and West Asturian-Leonese zones of the Iberian Massif.

Acknowledgements The authors warmly thank the useful and constructive remarks made by two anonymous referees, which greatly helped to improve the previous version of the manuscript. We thank J.L. Simón (Zaragoza University) for assisting with field work, the use of Servicio General de Apoyo a la Investigación-SAI (University of Zaragoza) and the facilities offered by J.R. Wijbrans at the $^{40}Ar/^{39}Ar$ Geochronology Laboratory of the Vrije Universiteit, Amsterdam. Financial support was provided by projects CGL2013-46169-C2-1-P and CGL2017-87631-P from Spanish MINECO, the Regional Government of Aragón and the European Regional Development Fund (Grupos Consolidados: Geotransfer and Recursos Minerales).

References

Ábalos, B., Carreras, J., Drugget, E., Escuder Viruete, J., Gómez Pugnaire, M. T., Lorenzo Álvarez, S., et al. (2002). Variscan and pre–Variscan tectonics. In W. Gibbons & T. Moreno (Eds.), *The geology of Spain* (pp. 155–183). London: Geological Society.

Aerden, D. G. A. M. (1994). Kinematics of orogenic collapse in the Variscan Pyrenees deduced from microstructures in porphyroblastic rocks from the Lys-Caillaous massif. *Tectonophysics, 238,* 139–160.

Álvaro, J. J. (1998). El Cámbrico Inferior y Medio en un sector de la Cadena Ibérica Occidental entre Villafeliche y Calamocha (margen derecha del río Jiloca, provincias de Zaragoza y Teruel). *Teruel, 86,* 7–42.

Álvaro, J. J., Bauluz, B., Gil Imaz, A., & Simón, J. L. (2008). Multidisciplinary constraints about Cadomian compression and early Cambrian extension in the Iberian Chains, NE Spain. *Tectonophysics, 491,* 215–227.

Álvaro, J. J., & Blanc-Valleron, M. M. (2002). Stratigraphic and structural framework of the Neoproterozoic Paracuellos Group, Iberian Chains, NE Spain. *Bulletin de la Société géologique de France, 173,* 27–35.

Álvaro, J. J., Elicki, O., Geyer, G., Rushton, A. W. A., & Shergold, J. H. (2003). Palaeogeographical controls on the Cambrian trilobite immigration and evolutionary patterns reported in the western Gondwana margin. *Palaeogeography, Palaeoclimatology, Palaeoecology, 195,* 5–35.

Álvaro, J. J., Liñán, E., & Pocoví, A. (1992). Un modelo alternativo al anticlinal del Manubles (Cadena Ibérica Occidental). *Geogaceta, 12,* 33–36.

Álvaro, J. J., & Vennin, E. (1998). Petrografía y diagénesis de las calizas cámbricas del Grupo Mesones (Cadenas Ibéricas, NE de España). *Boletín de la Real Sociedad Española de Historia Natural (Sección Geológica), 93,* 33–53.

Aparicio, A., Brell, J. M., & García, R. (1993). El metamorfismo hercínico de bajo a muy bajo grado en la Zona Cantábrica (Provincias de León, Asturias, Cantabria). *Boletín Geológico y Minero, 104,* 439–461.

Aparicio, A., Brell, J. M., García, R., Tena, J., & Gómez, J. (1991a). El metamorfismo de bajo grado en el Paleozoico del sector central de la Cordillera Ibérica. *Boletín Geológico y Minero, 102,* 735–747.

Aparicio, A., Brell, J. M., & Guaras, B. (1991b). El metamorfismo hercínico de la Sierra de la Demanda (provincias de Logroño y Burgos). *Boletín Geológico y Minero, 102,* 240–246.

Aramburu, C., Truyols, J., Arbizu, M., Méndez-Bedia, I., Zamarreño, I., García-Ramos, J. C., et al. (1992). El Paleozoico Inferior de la Zona Cantábrica. In J. C. Gutiérrez-Marco, J. Saavedra, & I. Rábano (Eds.), *Paleozoico Inferior de Ibero-América* (pp. 397–422). Mérida: UNEX Press.

Arenas, R., & Martínez Catalán, J. R. (2003). Low-P metamorphism following a Barrovian-type evolution. Complex tectonic controls for a common transition, as deduced in the Mondoñedo thrust sheet (NW Iberian Massif). *Tectonophysics, 365,* 143–164.

Ayati, F., Yavuz, F., Noghreyan, M., Haroni, A., & Yavuz, R. (2008). Chemical characteristics and composition of hydrothermal biotite from the Dalli porphyry copper prospect, Arak, central province of Iran. *Mineralogy and Petrology, 94,* 107–122.

Bastida, F., Brime, C., García-López, S., & Sarmiento, G. N. (1999). Tectonothermal evolution in a region with thin-skinned tectonics: the western nappes of the Cantabrian Zone (Variscan belt of NW Spain). *International Journal of Earth Sciences, 88,* 34–48.

Bauluz, B., Fernández Nieto, C., & González López, J. M. (1998). Diagenesis-very low grade metamorphism of clastic Cambrian and Ordovician sedimentary rocks in the Iberian Range (Spain). *Clay Minerals, 33,* 373–393.

Beane, R. E. (1974). Biotite stability in the porphyry copper environment. *Economic Geology, 69,* 241–256.

Calvín-Ballester, P., Casas, A. (2013). Folded Variscan thrusts in the Herrera Unit of the Iberian Range (NE Spain). In S. Llana-Fúnez, A. Marcos, F. Bastida (Eds.), Deformation Structures and Processes within the Continental Crust. Geological Society, London, Special Publication, 394, http://dx.doi.org/10.1144/SP394.3.

Capote, R., & González Lodeiro, F. (1983). La estructura hercínica en los afloramientos paleozoicos de la Cordillera Ibérica. Libro Jubilar J. M. Ríos. *IGME, 1,* 513–528.

Carls, P. (1983). La Zona Asturoccidental Leonesa en Aragón y el Macizo del Ebro como prolongación del Macizo Cantábrico. Libro Jubilar J. M. Ríos. *IGME, 3,* 11–32.

Carls, P., Gozalo, R., Valenzuela-Ríos, J. I., & Truyols-Massoni, M. (2004). La sedimentación marina devónico-carbonífera. In J. A. Vera (Ed.), *Geología de España* (pp. 475–479). Madrid: SGE-IGME.

Casas, A., Marcén, M., Calvín, P., Gil, A., Román, T., & Pocoví, A. (2016). Deformación varisca, tardivarisca y alpina en la Rama Aragonesa de la Cordillera Ibérica: propuesta para diferenciación y denominación de estructuras. *Geo-Temas, 16*(2), 495–498.

Casas Sainz, A. M., & Corés Gracia, A. L. (1996). Cabalgamientos plegados en el macizo hercínico de la Sierra de Herrera (Cordillera Ibérica). *Geogaceta, 19,* 3–6.

Casini, L., & Oggiano, G. (2008). Late orogenic collapse and thermal doming in the northern Gondwana margin incorporated in the Variscan Chain: A case study from the Ozieri Metamorphic Complex, northern Sardinia, Italy. *Gondwana Research, 13,* 396–406.

Colchen, M. (1974). Géologie de la Sierra de la Demanda (Burgos-Logroño, Espagne). *Memorias del IGME, 85,* 1–436.

Colomer, M., & Santanach, P. (1988). Estructura y evolución del borde suroccidental de la fosa de Calatayud-Teruel. *Geogaceta, 4,* 29–31.

Dallmeyer, R. D., Martínez Catalán, J. R., Arenas, R., Gil Ibarguchi, J. I., Gutiérrez-Alonso, G., Farias, P., et al. (1997). Diachronous Variscan tectonothermal activity in the NW Iberian Massif: Evidence from $^{40}Ar/^{39}Ar$ dating of regional fabrics. *Tectonophysics, 277,* 307–337.

García-López, S., Brime, C., Bastida, F., & Sarmienot, G. (1997). Simultaneous use of thermal indicators to analyze the transition from diagenesis to metamorphism: an example from the Variscan Belt of Northwest Spain. *Geological Magazine, 134,* 323–334.

García-López, S., Brime, C., Valón, M. L., Sanz-López, J., Bastida, F., Aller, J., et al. (2007). Tectonothermal evolution of a foreland fold and thrust belt: The Cantabrian Zone (Iberian Variscan belt, NW Spain). *Terra Nova, 19,* 469–475.

Gozalo, R., & Liñán, E. (1988). Los materiales hercínicos de la Cordillera Ibérica en el contexto del Macizo Ibérico. *Estudios Geológicos, 44,* 399–404.

Guidotti, C. V. (1984). Micas in metamorphic rocks. In S.W. Bailey (Ed), Micas. Reviews in Mineralogy, 13, 357–467.

Gutiérrez-Alonso, G. (2004). La transición de la Zona Asturoccidental-Leonesa con la Zona Cantábrica: el Antiforme del Narcea. In J. A. Vera (Ed.), *Geología de España* (pp. 52–54). Madrid: SGE-IGME.

Hernández Samaniego, A., Olivé Davó, A., Pardo Tirapu, G., Villena Morales, J., Moissent, E. (1980a). Mapa Geológico de España, 1:50.000 Sheet no. 491 (Calamocha). IGME, Madrid.

Hernández Samaniego, A., Olivé Davó, A., Sdzudy, K., Kolb, S. (1980b). Mapa Geológico de España, 1:50.000 Sheet no. 465 (Daroca). IGME, Madrid.

Julivert, M. (1954). Observaciones sobre la tectónica de la Depresión de Calatayud. *Arrahona, 18,* 3–18.

Julivert, M., Fontboté, J. M., Ribeiro, A., & Conde, L. (1972). *Mapa tectónico de la Península Ibérica y Baleares*. Madrid: Instituto Geológico y Minero de España.

Julivert, M., Pello, J., & Fernández-García, L. (1968). La estructura del Manto de Somiedo (Cordillera Cantábrica). *Trabajos de Geología, 2,* 1–44.

Kuiper, K. F., Deino, A., Hilgen, F. J., Krijgsman, W., Renne, P. R., & Wijbrans, J. R. (2008). Synchronizing the rock clocks of Earth History. *Science, 320,* 500–504.

Lago, M., Arranz, E., Pocoví, A., Galé, C., Gil-Imaz, A. (2004). Lower Permian magmatism of the Iberian Chain, Central Spain, and its relationship to extensional tectonics. In M. Wilson, E. R. Neumann, G. R. Davies, M. J. Timmerman, M.Heeremans, B. T. Larsen (Eds.), Permo–Carboniferous Magmatism and Rifting in Europe. Geological Society, London, Special Publications, vol. 223, pp. 465–491.

Ledru, P., Courrioux, G., Dallain, C., Lardeaux, J. M., Montel, J. M., Canderhaeghe, O., et al. (2001). The Velay dome (French Massif Central): melt generation and granite emplacement during orogenic evolution. *Tectonophysics, 342,* 207–237.

Lendínez González, A., Ruiz Fernández, V., Carls, P. (1989). Mapa Geológico de España. Sheet no. 466, Moyuela. IGME, Madrid.

Liesa, C. L., & Casas Sáinz, A. M. (1994). Reactivación alpina de pliegues y fallas del zócalo hercínico de la Cordillera Ibérica: ejemplos de la Sierra de la Demanda y la Serranía de Cuenca. *Cuadernos do Laboratorio Xeolóxico de Laxe, 19,* 119–135.

López-Gómez, J., Arche, A., & Pérez-López, A. (2002). Permian and Triassic. In W. Gibbons & T. Moreno (Eds.), *The Geology of Spain*. London: Geological Society.

Lotze, F. (1929). Stratigraphie und Tektonic des keltiberischen Grundgebirges (Spanien). *Abhandlungen der Gessellschaft für Mathematisch-physikalische Klasse (neue Folge), 14,* 1–320.

Mandado, J., & Tena, J. (1991). Los depósitos areníticos del Cámbrico Inferior de la Unidad de Mesones (Cadena Ibérica Oriental). Análisis petrográfico de proveniencia de materiales. *Cuadernos do Laboratorio Xeolóxico de Laxe, 16,* 125–134.

Martín Fernández, M., Canerot, J., Linares-Rivas, A. (1977). Mapa Geológico de España, 1:50.000 Sheet no. 492 (Segura de los Baños). IGME, Madrid.

Martínez Catalán, J. R. (1985). Estratigrafía y estructura del Domo de Lugo (sector Oeste de la Zona Asturoccidental-Leonesa). *Corpus Geologicum Gallaeciae, 2,* 1–291.

Martínez Catalán, J. R., Arenas, R., Díaz García, F., Gómez Barreiro, J., González Cuadra, P., Abati, J., Castiñeiras, P., Fernández-Suárez, J., Sánchez Martínez, S., Andonaegui, P., González Clavijo, E., Díez Montes, A., Rubio Pascual, F. J., Valle Aguado, B. (2007). Space and time in the tectonic evolution of the northwestern Iberian Massif. Implications for the Variscan belt. In R. D. Hatcher, M. P. Carlson, J. H. McBride, J. R. Martínez Catalán (Eds.), 4-D Framework of Continental Crust (pp. 403–423). Geological Society of America Memoir, Boulder, Colorado.

Martínez Catalán, J. R., Pérez Estaún, A., Bastida, F., Pulgar, J. A., & Marcos, A. (1990). Structure: West Asturian-Leonese Zone. In R. D. Dallmeyer & E. Martínez-García (Eds.), *Pre-Mesozoic Geology of Iberia* (pp. 103–114). Berlin: Springer.

Martínez Catalán, J. R., Rubio Pascual, F. J., Díez Montes, A., Díez Fernández, R., Gómez-Barreiro, J., Dias da Silva, I., González Clavijo, E., Ayarza, P., Alcock, J.E. (2014). The late Variscan HT/LP metamorphic event in NW and Central Iberia: relationships to crustal thickening, extension, orocline development and crustal evolution. In K. Schulmann, J. R. Martínez Catalán, J. M. Lardeaux, V. Janoušek, G. Oggiano (Eds.), The Variscan Orogeny: Extent, Timescale and the Formation of the European Crust. Geological Society of London, Special Publication, 405, 225–247.

Martínez, F. G., Julivert, M., Sébastien, A., Arboleya, M. L., & Dietsch, C. (1988). Structural and thermal evolution of high-grade areas in northwestern parts of the Iberian massif. *American Journal of Sciences, 288,* 969–996.

McDougall, I., & Harrison, T. M. (1999). *Geochronology and Thermochronology by the $^{40}Ar/^{39}Ar$ method* (p. 212). New York: Oxford University Press.

Nance, R. D., Gutiérrez-Alonso, G., Keppie, J. D., Linnemann, U., Murphy, J. B., Quesada, C., et al. (2012). A brief history of the Rheic Ocean. *Geoscience Frontiers, 3,* 125–135.

Nance, R. D., & Linnemann, U. (2009). The Rheic Ocean: Origin, evolution and significance. *GSA Today, 18*(12), 4–12.

Navarro Vázquez, D. (1991). Cabalgamientos hercínicos en la Unidad de Herrera (Rama Oriental del Macizo Paleozoico de la Cordillera Ibérica). *Boletín Geológico y Minero, 102,* 830–837.

Navas, A., & Tena, J. (1988). Caracteres petrológicos y estructuras del Paleozoico de las sierras de Vicort y Algairén (Prov. de Zaragoza). *Boletín Geológico y Minero, 99,* 647–659.

Pérez-Estaún, A. (1978). Estratigrafía y estructura de la rama Sur de la Zona Asturoccidental-Leonesa. *Memorias del IGME, 92,* 1–149.

Pérez-Estaún, A., & Bastida, F. (1990). Structure: Cantabrian Zone. In R. D. Dallmeyer & E. Martínez-García (Eds.), *Pre-Mesozoic Geology of Iberia* (pp. 55–69). Berlin: Springer.

Pérez-Estaún, A., Bastida, F., Alonso, J. L., Marquínez, J., Aller, J., Álvarez-Marrón, J., et al. (1988). A thin-skinned tectonics model for an arcuate fold and thrust belt: The Cantabrian Zone (Variscan Ibero-Armorican Arc). *Tectonics, 7,* 517–537.

Pérez-Estaún, A., Martínez Catalán, J. R., & Bastida, F. (1991). Crustal thickening and deformation sequence in the footwall to the suture of the Variscan belt of northwest Spain. *Tectonophysics, 181,* 243–253.

Pérez-Lorente, F. (1990). Datos tectónicos de un área alrededor de Mesones de Isuela e Illueca (Provincia de Zaragoza, Cordillera Ibérica). *Boletín de la Real Sociedad Española de Historia Natural (Sección Geológica), 85,* 23–43.

Renne, P. R., Deino, A. L., Hames, W. E., Heizler, M. T., Hemming, S. R., Hodges, K. V., et al. (2009). Data reporting norms for $^{40}Ar/^{39}Ar$ geochronology. *Quaternary Geochronology, 4,* 346–352.

Rubio Pascual, F. J., Arenas, R., Martínez Catalán, J. R., Rodríguez Fernández, L. R., & Wijbrans, J. R. (2013). Thickening and exhumation of the Variscan roots in the Spanish Central System: Tectonothermal processes and $^{40}Ar/^{39}Ar$ ages. *Tectonophysics, 587,* 207–221.

Ruiz Fernández, V., Carls, P. (1985). Mapa Geológico de España, 1:50.000 Sheet no. 466 (Moyuela). IGME, Madrid.

Sächer, L. (1966). Uber Karbonische Sedimente bei Montalbán in den Östlichen Iberischen Ketten (Spanien). *Neues Jahrbuch für Geologie und Palaöntologie, Monatshefte, 7,* 437–443.

Sanz, T., Lago, M., Gil, A., Galé, C., Ramajo, J., Ubide, T., et al. (2013). The Upper Triassic alkaline magmatism in the NW Iberian Chains (Spain). *Journal of Iberian Geology, 39,* 203–222.

Schuevens, D. (2002). Metamorphism and microstructures along a high-temperature metamorphic field gradient: the north-eastern boundary of the Královský hvozd Unit (Bohemian Massif, Czech Republic). *Journal of Metamorphic Geology, 20,* 413–428.

Suárez, O., Corretge, L. G., Martínez, F. J. (1990). Distribution and characteristics of the Hercynian metamorphism. Part III. West Asturian-Leonese Zone. In R. D. Dallmeyer, E. Martínez García (Eds.), Pre–Mesozoic Geology of Iberia (pp. 129–133). Springer, Berlin.

Tejero, R., & Capote, R. (1987). La deformación hercínica de los macizos paleozoicos nororientales de la Cordillera Ibérica. *Estudios Geológicos, 43,* 425–434.

Tejero, R., & de Vicente, G. (1987). Análisis cuantitativo de la fracturación tardihercínica en la Rama Aragonesa de la Cordillera Ibérica. *Geogaceta, 2,* 14–17.

Tischendorf, G., Gottesmann, B., Förster, H. J., & Trumbull, R. B. (1997). On Li-bearing micas: estimating Li from electron microprobe analysis and an improved diagram for graphical representation. *Mineralogical Magazine, 61,* 809–834.

Ubide, T., Wijbrans, J. R., Galé, C., Arranz, E., Lago, M., & Larrea, P. (2014). Age of the Cretaceous alkaline magmatism in northeast Iberia: implications for the Alpine cycle in the Pyrenees. *Tectonics, 33*(7), 1444–1460.

Villa, E., Escuder, J., & van Ginkel, A. C. (1996). Fusulináceos y edad de los afloramientos carboníferos de Puig Moreno (Cordillera Ibérica, Teruel, España). *Revista Española de Paleontología, 11,* 207–215.

Villena, J., Pardo, G. (1983). El Carbonífero de la Cordillera Ibérica. In C. Martínez Díaz (Ed.), Carbonífero y Pérmico de España (pp. 189–206). IGME, Madrid.

Von Raumer, J., & Stampfli, G. M. (2008). The birth of the Rheic Ocean—Early Paleozoic subsidence patterns and tectonic plate scenarios. *Tectonophysics, 461,* 9–20.

Affiliations

J. Javier Álvaro[1] · Blanca Bauluz[2] · Andrés Gil-Imaz[2] · Teresa Ubide[3]

✉ J. Javier Álvaro
jj.alvaro@csic.es

Blanca Bauluz
bauluz@unizar.es

Andrés Gil-Imaz
agil@unizar.es

Teresa Ubide
t.ubide@uq.edu.au

[1] Instituto de Geociencias (CSIC-UCM), Dr. Severo Ochoa 7, 28040 Madrid, Spain

[2] Departamento Ciencias de la Tierra, Instituto de Investigación en Ciencias Ambientales (IUCA), Universidad de Zaragoza, 50009 Saragossa, Spain

[3] School of Earth and Environmental Sciences, The University of Queensland, Brisbane, QLD 4072, Australia